01 Apr 2022

Local Prediction of Laser Powder Bed Fusion Porosity by Short-Wave Infrared Imaging Thermal Feature Porosity Probability Maps

Cody S. Lough

Tao Liu

Xin Wang

Ben Brown

et. al. For a complete list of authors, see https://scholarsmine.mst.edu/mec_aereng_facwork/4944

Recommended Citation

C. S. Lough et al., "Local Prediction of Laser Powder Bed Fusion Porosity by Short-Wave Infrared Imaging Thermal Feature Porosity Probability Maps," *Journal of Materials Processing Technology*, vol. 302, article no. 117473, Elsevier, Apr 2022.
The definitive version is available at https://doi.org/10.1016/j.jmatprotec.2021.117473

Journal of Materials Processing Tech. 302 (2022) 117473

Contents lists available at ScienceDirect

Journal of Materials Processing Tech.

journal homepage: www.elsevier.com/locate/jmatprotec

Local prediction of Laser Powder Bed Fusion porosity by short-wave infrared imaging thermal feature porosity probability maps

Cody S. Lough [a,b], Tao Liu [a], Xin Wang [a], Ben Brown [b], Robert G. Landers [c], Douglas A. Bristow [a], James A. Drallmeier [a], Edward C. Kinzel [c,*]

[a] Department of Mechanical and Aerospace Engineering, Missouri University of Science and Technology, Rolla, MO 65409, United States
[b] Kansas City National Security Campus, Kansas City, MO 64147, United States[1]
[c] Department of Aerospace and Mechanical Engineering, University of Notre Dame, Notre Dame, IN 46556, United States

ARTICLE INFO

Associate Editor: Adam Thomas Clare

Keywords:
Laser Powder Bed Fusion
SWIR
Porosity detection
Receiver operating characteristic

ABSTRACT

Local thermal history can significantly vary in parts during metal Additive Manufacturing (AM), leading to local defects. However, the sequential layer-by-layer nature of AM facilitates in-situ part voxelmetric observations that can be used to detect and correct these defects for part qualification and quality control. The challenge is to relate this local radiometric data with local defect information to estimate process error likelihood in future builds. This paper uses a Short-Wave Infrared (SWIR) camera to record the temperature history for parts manufactured with Laser Powder Bed Fusion (LPBF) processes. The porosity from a cylindrical specimen is measured by ex-situ micro-computed tomography (μCT). Specimen data from the SWIR camera, combined with the μCT data, are used to generate thermal feature-based porosity probability maps. The porosity predictions made by various SWIR thermal feature-porosity probability maps of a specimen with a complex geometry are scored against the true porosity obtained via μCT. The receiver operating characteristic curves constructed from the predictions for the complex sample demonstrate the porosity probability mapping methodology's potential for in-situ based porosity detection.

1. Introduction

The expanding presence of metal Additive Manufacturing (AM) in industry has increased the need for qualification of parts with geometric complexities beyond what are typically produced using traditional manufacturing processes. Laser Powder Bed Fusion (LPBF) is an established AM technology that fabricates intricate part geometries with high resolutions by leveraging melt pool sizes, powder diameters, and layer thicknesses all on the length scale of tens of microns. Laser Powder Bed Fusion manufactured parts experience significant thermal variations at a local level due to changing scan pathing and heat transfer boundary conditions. Defects (e.g., lack of fusion, keyholing porosity, balling) depend on the melting modes and are challenging to completely eradicate by laser parameter and beam path optimization due to the complex thermal variations experienced throughout a part. The layer-to-layer material addition in LPBF permits the ability to interrogate the thermal history at every point in a part through in-situ radiometry. The information obtained from these non-contact measurements correlates with the part's local thermal history and, thus, its material quality. This correlation enables radiometric techniques to identify the locations of thermal variances in parts that have a high probability for defects such as porosity. The development of local part property prediction maps based on thermal measurements allows microstructure state estimation to aid the qualification of mission critical parts.

Porosity has been extensively studied in LPBF due to the difficulties in eliminating it entirely from the manufacturing process and the negative impacts it has on part mechanical performance. Two types of laser parameter driven porosity exist and are classified based on the dynamics leading to its formation. These include lack of fusion/incomplete melting, where porosity occurs due to insufficient energy to melt the powder particles, and over melting which is associated with the formation of keyholes and their collapse. Gong et al. (2014) defined processing regimes for LPBF of Ti-6Al-4V according to the resulting porosity/defect type. Generally, a porosity level of less than 0.1 % is

* Corresponding author.
E-mail address: ekinzel@nd.edu (E.C. Kinzel).

[1] The Department of Energy's Kansas City National Security Campus is operated and managed by Honeywell Federal Manufacturing & Technologies, LLC under contract number DE-NA0002839.

https://doi.org/10.1016/j.jmatprotec.2021.117473
Received 10 September 2021; Received in revised form 15 December 2021; Accepted 19 December 2021
Available online 21 December 2021

considered the fully dense regime (Gordon et al., 2020). Similar studies by King et al. (2014) implemented a normalized enthalpy calculation to determine where the fully dense regime transitioned to keyholing and applied this analysis to single laser track experiments. Wang et al. (2021) showed that an analytical Rosenthal type solution with powder packing information can be used to estimate melt pool dimensions and provide insight into lack of fusion porosity. Promoppatum et al. (2022) used a comparable numerical approach to predict porosity and found a strong correlation between their predictions and experimental porosity measured ex-situ. Recently, several groups, including Hojjatzadeh et al. (2020), have used in-situ synchrotron based high speed X-ray imaging to study the various phenomenon leading to porosity in LPBF. While these studies help to understand the process physics and resulting defect formation, in practice it is not economically viable to implement these as sensing systems in standard industrial applications.

Many studies have pursued in-situ inspection of LPBF toward process validation. This includes the use of a wide range of radiometric signals including visible and infrared imaging, pyrometers, photodiodes, and spectrometers to measure various aspects of the LPBF process. The apparent melt pool geometry, intensity/temperature, and laser spatter measured by these instruments can all be correlated with process quality. For example, Craeghs et al. (2012) demonstrated that the melt pool area from Near Infrared imaging can be used to indicate part failures and Krauss et al. (2014) evaluated how averaged mapped measurements progress layer-wise. Methods implementing thermography and pyrometry have identified embedded voids and naturally occurring porosity in powder bed fusion AM parts. Mireles et al. (2015) acquired infrared camera images to detect various geometry voids down to 600 μm designed into a part manufactured by Electron Beam Melting (EBM). Similarly, Taherkhani et al. (2021) used photodiodes to identify artificial lack of fusion defects down to a minimum designed volume of 120 μm with a detection rate up to 73 %. In an in-situ measurement and thermal model hybrid approach, Yavari et al. (2021) combined photodiode data with graph theory simulated temperature fields to identify pores in parts down to 100 μm. Bartlett et al. (2018) used Long-Wave Infrared (LWIR) images captured after the raster in LPBF to identify subsurface defects for samples manufactured with baseline and porosity promoting parameters. Yoder et al. (2019) demonstrated that features in voxel reconstructions based on static Near Infrared (NIR) images captured after each layer correlate to porosity resulting from a decrease in layer-to-layer time in EBM of Ti-6Al-4V. Mitchell et al. (2020) detected voids manufactured within an LPBF part down to 120 μm by volumetric reconstructions of thermal data and successfully correlated locations of natural porosity with outlier melt pool images through two-color pyrometry. Mohr et al. (2020) found a significant overlap (~71 %) between micro-computed tomography (μCT) measured porosity and anomalies in voxelized thermal feature data. Coeck et al. (2019) demonstrated the porosity prediction potential using two photodiodes. Perfect defect prediction has proven elusive. For example, the framework presented by Coeck et al. (2019) identified 54 out 93 pores with 61 false positives based on micro-CT data in a Ti-6Al-4V part created with LPBF. Forien et al. (2020) studied the correlation between in-situ pyrometry measurements and porosity obtained by ex-situ X-ray imaging for single laser scans of 316 L stainless steel. They used the pyrometry and the porosity data for various laser parameters to build pyrometer signal distributions corresponding to nominal material and pores. The distributions define the probability that keyholing porosity occurs based on a single laser scan's pyrometry data. This framework is promising for porosity prediction in single laser scans, but the capability to apply the methodology for predictions in 3D parts is unknown.

This paper investigates the probabilistic prediction of porosity using in-situ Short-Wave Infrared (SWIR) based thermographic imaging. A framework similar to what Forien et al. (2020) suggested for single laser scan data is established to produce statistical maps between voxelized SWIR thermal features and micro-CT measured porosity for 3D parts. The SWIR camera used in the work conducted in this paper has a high sensitivity at wavelengths corresponding to the peak emission at the melting temperature of stainless steel, which is the material used in this study, making it suitable to capture porosity formation signatures. Recording the spatial and temporal components of the LPBF thermal history allows multiple features to be included for porosity prediction. This goes beyond the information provided by single point intensities from photodiodes, or single images captured from layers post fusion. In this paper, data are measured during the fabrication of samples with simple geometries using a range of process parameters that span the thermal feature space. This produces two-feature process probability maps for porosity generated from lack of fusion and keyholing modes. These maps are shown to predict the porosity in samples with complex geometries created using nominal processing conditions where the defects are introduced due to geometry-induced changes in the thermal history. A comparison with μCT ground truth data is used to assess the porosity probability maps' predictions for the sample with complex geometries.

2. Experimental methods

2.1. LPBF system and sample descriptions

This study uses a Renishaw AM250 LPBF system to process 304 L stainless steel powder. The AM250 employs an SPI Lasers fiber laser (maximum power $P_{max} = 200$ W and wavelength $\lambda = 1070$ nm) to build parts with a point-to-point exposure strategy. A cylindrical sample and a complex sample with geometries shown in Fig. 1(a) are fabricated for this study. The cylindrical sample's diameter is 4 mm and it has 20 sections, each 20 layers thick. The layer height is 50 μm.

Randomized combinations of laser power, $P = 100–200$ W (25 W increments) and exposure time, $t_e = 50–125$ μs (25 μs increments) process the sample's various sections. The process parameters are varied to quickly produce a comprehensive set of sample properties spanning the lack of fusion porosity, keyholing porosity, and fully dense processing regimes. The laser scans the cylindrical sample's layers using a raster pattern that rotates 67 ° every layer and two border scans after the raster scan. The raster pattern has a constant point distance, $d_p = 60$ μm, and a constant hatch spacing, $d_h = 85$ μm. The different raster vector lengths in the cylindrical sample's layers cause natural thermal variations in addition to laser parameter driven thermal variances. The complex sample shown in Fig. 1(a) consists of a 2.5 mm tall rectangular cross-section that is 7×8 mm^2 and a 2.5 mm tall equilateral triangular cross-section with 8 mm side lengths (bulk section), and two 4.3 mm tall triangular pyramid structures with 8 mm base side lengths and 45 ° face angles (inverted half of pyramid is denoted overhang section and upright half of pyramid is denoted supported section). A single fully dense

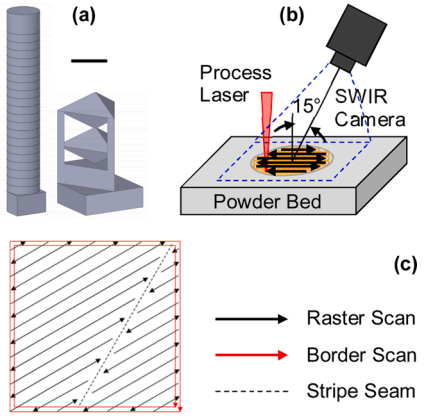

Fig. 1. (a) Cylindrical sample and complex sample CAD models, (b) SWIR camera observation of the LPBF process, and (c) laser scan path schematic showing raster vector stripes and border vectors. Scale bar, 5 mm.

regime parameter set ($P = 200$ W, $t_e = 75$ μs) and scan path striping are used to manufacture the complex sample. Note the cylindrical sample is manufactured without striping. Scan path striping, illustrated in Fig. 1 (c), is the division of a layer's cross-sectional area into shorter sets of laser raster vectors. As a result, the laser corners in the sample's interior and seams occur where the stripes overlap. The striping orientations and seam positions change from layer-to-layer, producing laser raster vector length and cornering dwell location differences. This combined with the complex sample's geometry dependent heat transfer boundary conditions (i.e., supported or overhang), induces natural thermal history variations.

2.2. In-situ SWIR camera and calibration procedure

A FLIR SC6201 Short Wave Infrared (SWIR) InGaAs camera images the build plate from a staring configuration. The spatiotemporal melt pool emission data is recorded layer-by-layer for the samples through a custom window (schematic of camera configuration in Fig. 1(b)). A band pass filter centered at 1.45 μm (Edmund Optics #85-913) prevents saturation of the SWIR camera. The 640 × 512 focal plane array camera's 130 μm/pixel x-direction and 135 μm/pixel y-direction instantaneous field of view produces an 83 × 69 mm^2 total field of view. The camera records the spatiotemporal data for the samples with an integration time of 5 μs at a frame rate of 2585 Hz by windowing to 80 × 80 pixels.

The SWIR camera measures the melt pool's emission in arbitrary units. A Non-Uniformity Correction (NUC) accounts for the emission signal's cosine dependence from measurements at ~15 ° off normal and vignetting caused by the viewing window. A combination of experimental blackbody temperature data and theoretical Planck distribution exitance data was used to calibrate the SWIR measurements into units of temperature. The Renishaw's process laser heated an LPBF manufactured blackbody for the calibration experiment. Thermocouples measured the blackbody's temperature and the SWIR camera simultaneously recorded raw radiation. Integrating the Planck distribution over the camera's observation wavelengths provides the theoretical blackbody exitance at a given temperature. The theoretical blackbody exitance from this integration scales with temperature to the 5.6th power. This relationship, combined with the thermocouple measurements, allows calculation of the theoretical exitance emitted by the blackbody. The results show the SWIR camera's raw radiation measurements linearly transform to the theoretical blackbody exitance. The theoretical temperature-exitance inverse relationship calibrates the camera's exitance data to temperature. This calibration assumes a constant emissivity of one for the 304 L stainless steel, neglecting the temperature and phase dependence. The calibrated SWIR data is reported as the equivalent blackbody temperature, denoted T_{BB}.

2.3. SWIR thermal feature extraction

Fig. 2(a–c) show example temperature calibrated spatiotemporal SWIR data from a fully dense regime layer ($P = 200$ W, $t_e = 75$ μs) in the cylindrical sample. The data in Fig. 2(a–c) are the temperatures as a function of time plotted relative to their times at local maximum temperature and the melt pool images at maximum temperature for three pixels along a laser scan vector. The plots demonstrate the variances in the layer's temperature history and melt pool profiles measured by the SWIR camera as the laser progresses from cornering in Fig. 2(a) to the end of a scan vector in Fig. 2(c). The SWIR camera captures megabytes of thermal data per layer, resulting in gigabytes of data for the entire sample. Thermal features are extracted from the SWIR measurements to compress them and produce 3D voxel data for a sample to efficiently make decisions. Thermal features are physics-based metrics that quantitatively describe process phenomena like those observable in Fig. 2 (a–c) via the reduction of a layer's spatiotemporal SWIR data to a single measure per pixel.

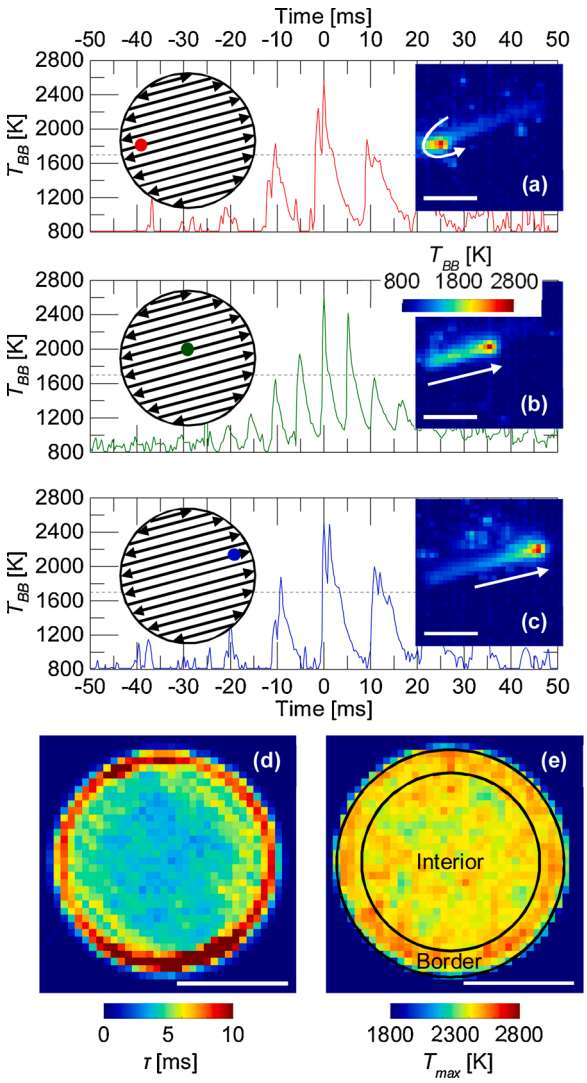

Fig. 2. Spatiotemporal SWIR measurements from laser scan vector's (a) beginning, (b) middle, and (c) end for cylindrical sample's layer 400 processed with $P = 200$ W and $t_e = 75$ μs with (d) time above threshold (1700 K) and (e) maximum temperature thermal feature maps. When the laser is at the pixel, $t = 0$. Scale bars, 2 mm.

A number of thermal features have been proposed in the literature including temperature-based metrics like the maximum temperature (Krauss et al., 2014) and cooling rates (Heigel and Whitenton, 2018), and melt pool geometry related features like the melt pool's dimensions (Cheng et al., 2018) and the time above threshold (Mohr et al., 2020). The temperature-based metrics and the melt pool geometry related features are acquired by either single point/frame measures, or an inclusion of spatiotemporal effects. For example, the maximum temperature and the maximum cooling rate are both temperature-based metrics, but the maximum temperature is a single point measure, and the maximum cooling rate relies on temporal information. Additionally, the melt pool area is a feature based on a single frame while the time above threshold temporally captures the melt pool geometry information. Even though the single point features and the spatiotemporal effects features are based on different amounts of data, they are all shown to strongly correlate with the bulk yield strength and porosity of LPBF fabricated 304 L stainless steel when extracted from SWIR data (Lough et al., 2020). This study uses the features of the maximum temperature, T_{max}, (i.e., a pixel's temporal maximum during a layer's fabrication) and the time above threshold, τ, (i.e., the total time a pixel measures above a set temperature during a layer's fabrication). These features are selected to

evaluate the extension of the capabilities of a feature representing the single point measures in T_{max} and a feature representing the inclusion of spatiotemporal effects in τ extracted at thresholds ranging from 1100 K to 2100 K, and their combination, to locally predict the probability that porosity occurs in a part. The time above threshold using 1700 K and maximum temperature for the fully dense regime layer are plotted in Fig. 2(d) and (e), respectively, to demonstrate the thermal features.

2.4. Micro-computed tomography and thermal feature data registration

Micro-computed tomography (μCT) scanning establishes the porosity ground truth for the samples. The μCT X-ray image slices' gray scale intensities correlate to beam attenuation. The sample's porosity reduces the beam's attenuation which indicates a relative density decrease. The relative density slices combine to form 3D voxel data for a sample. The μCT data sets in this study have a voxel resolution of 15 μm/pixel in the x-y plane and 10 μm/pixel in the z-direction.

Fig. 3 shows the steps used to classify the SWIR thermal feature voxel data based on the sample's porosity measured by μCT. The first step down-samples the raw μCT data to the SWIR data resolution by averaging and simultaneously produces a respective binary sample state map. The binary map's states include porosity (white) and fully dense (black). A down-sampled voxel is porosity in the binary map if more than 5 % of the original resolution data within that voxel corresponds to porosity, flagging the fine porosity features observable in the original μCT data. The second step (not shown in Fig. 3) is manual build direction (z-direction) alignment of the data sets. The third step automatically registers the SWIR data with the down sampled μCT data in the x-y plane through translations layer-by-layer. The final step classifies the registered thermal feature voxels as porosity or fully dense based on the μCT data binary state map. For example, if the voxel in the μCT data binary map at a given (x,y,z) is porosity, then the SWIR thermal feature at the same (x,y,z) is classified as porosity. The registered SWIR voxels are separated and labeled according to their classification (i.e., porosity or fully dense) for the layer in Fig. 3 to clearly show the classification result. Once classified, the thermal feature data are used to produce probability density functions for all the voxels.

2.5. Thermal feature porosity probability map generation

The probability density functions obtained from the cylindrical sample's classified SWIR data are used to construct thermal feature porosity probability maps. Thermal feature porosity probability maps define the probability that porosity forms in a sample based on the sample's thermal feature measurements. The probability of porosity mapping, denoted φ, given a time above threshold, τ, is

$$P(\varphi|\tau) = \frac{P(\varphi \cap \tau)}{P(\tau)}, \tag{1}$$

where $P(\varphi \cap \tau)$ is the probability density function of the porosity and the time above threshold intersection and $P(\tau)$ is the probability density function of the time above threshold. The bin size for the time above threshold probability density functions is 0.5 ms. The probability of porosity mapping given a maximum temperature, T_{max}, is

$$P(\varphi|T_{max}) = \frac{P(\varphi \cap T_{max})}{P(T_{max})}, \tag{2}$$

where $P(\varphi \cap T_{max})$ is the probability density function of the porosity and the maximum temperature intersection and $P(T_{max})$ is the probability density function of the maximum temperature. The bin size for the maximum temperature probability density functions is 15 K. Combining time above threshold and maximum temperature measurements produces 2D thermal feature space porosity probability maps. The probability of porosity mapping given a time above threshold and maximum temperature is

$$P(\varphi|\tau \cap T_{max}) = \frac{P(\varphi \cap \tau \cap T_{max})}{P(\tau \cap T_{max})}, \tag{3}$$

where $P(\varphi \cap \tau \cap T_{max})$ is the probability density function of the porosity, time above threshold, and the maximum temperature intersection and $P(\tau \cap T_{max})$ is the probability density function of the time above threshold and the maximum temperature intersection.

While not all plotted in this paper for brevity, the thermal feature extraction, registration, and probability map generation procedures produced single feature porosity probability maps and 2D feature space porosity probability maps based on the cylindrical sample's time above threshold extracted at various temperatures (1100−2100 K) and the maximum temperature. Spatial filtering separates the cylindrical sample's interior and border data to construct unique thermal feature porosity probability maps for each region. The unique maps are constructed because of the differences in the process dynamics where the laser corners during rastering and border scans. The three outermost voxels in the cylindrical sample's thermal feature data correspond to the

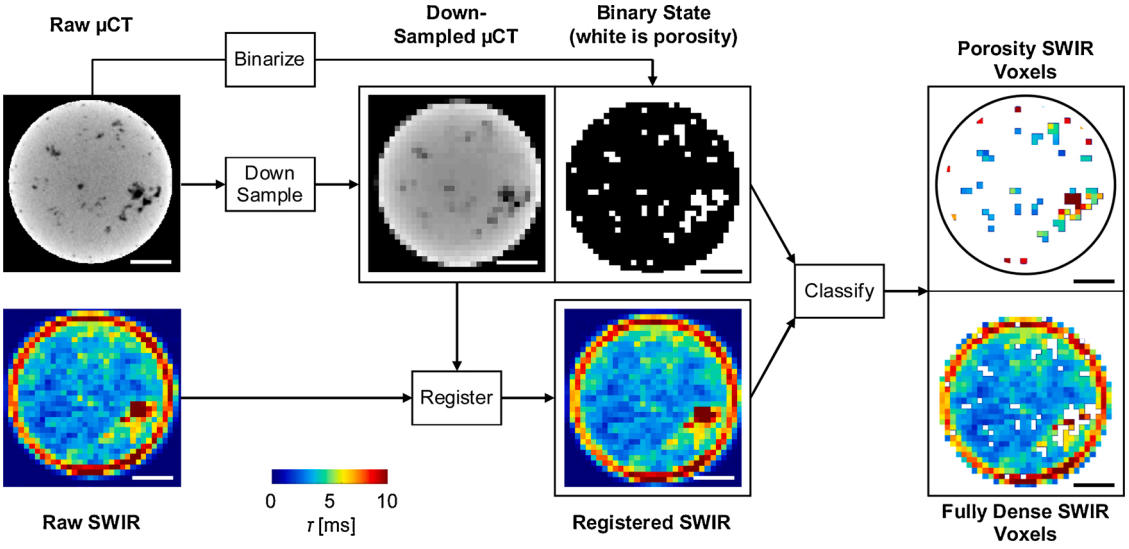

Fig. 3. Procedure for voxel-by-voxel classification of time above 1700 K thermal feature measurements as porosity or fully dense based on μCT data. Scale bars, 1 mm.

laser cornering and border scan location and, thus, define the part border. The interior and border regions are highlighted on the maximum temperature plot in Fig. 2(e).

2.6. Porosity probability prediction

The porosity probability maps are applied to make predictions for the complex sample to analyze the methodology's performance. The probability map-based predictions assume that the thermal history experienced during a sample's layer is the most critical factor in porosity formation and, thus, neglects layer-to-layer effects. This approach is supported by Gould et al. (2021) finding that a layer's in-situ thermography data relates to the resulting pores via simultaneous thermographic and synchrotron radiation inspection. The thermal feature porosity probability maps make predictions for the complex sample voxel-by-voxel by computing the expected porosity given its thermal feature measurements. Both the interior and the border thermal feature porosity probability maps predict the complex sample's porosity, where the border map only applies to the three outermost voxels within the sample's layers. The prediction framework saturates voxels with measurements that fall outside of the maps' thermal feature space (i.e., the full thermal feature range seen in the cylindrical sample's measurements).

An operating point transforms the porosity probability predictions into binary measurements for voxel-by-voxel scoring with the ground truth from μCT data. Predictions falling below the operating point are fully dense, and predictions above are porosity. Comparing the converted prediction data with the binary μCT data ground truth provides the true positives, T_p, (i.e., prediction and truth are both porosity), false positives, F_p, (i.e., prediction is porosity, but truth is no porosity), true negatives, T_n, (i.e., prediction and truth are both no porosity), and false negatives, F_n, (i.e., prediction is no porosity, but truth is porosity). Calculations based on those metrics yield the true positive and false positive rates. The true positive rate, R_t, is

$$R_t = \frac{T_p}{T_p + F_n}, \tag{4}$$

and the false positive rate, R_f, is

$$R_f = \frac{F_p}{F_p + T_n}. \tag{5}$$

Sweeping the operating point over a range and calculating the respective prediction rates generates a Receiver Operating Characteristic (ROC) curve for a porosity probability map. The ROC curve is a plot of the true positive rate against the false positive rate. A common way to quantify the overall prediction performance is by calculating the area under the ROC curve (AUC).

3. Results and discussion

3.1. Cylindrical sample micro-computed tomography and thermal feature data

Fig. 4 compares the cylindrical sample's μCT data with the corresponding SWIR imaging results. The μCT data and time above threshold (1700 K) for the cylindrical sample's cross-section are plotted in Fig. 4 (a) and (b), respectively, and highlight sections that correspond to the fully dense, keyholing, and lack of fusion processing regimes. The correlations between thermal features and porosity are analyzed locally for the three processing regimes in Fig. 4(c–e), where μCT data and time

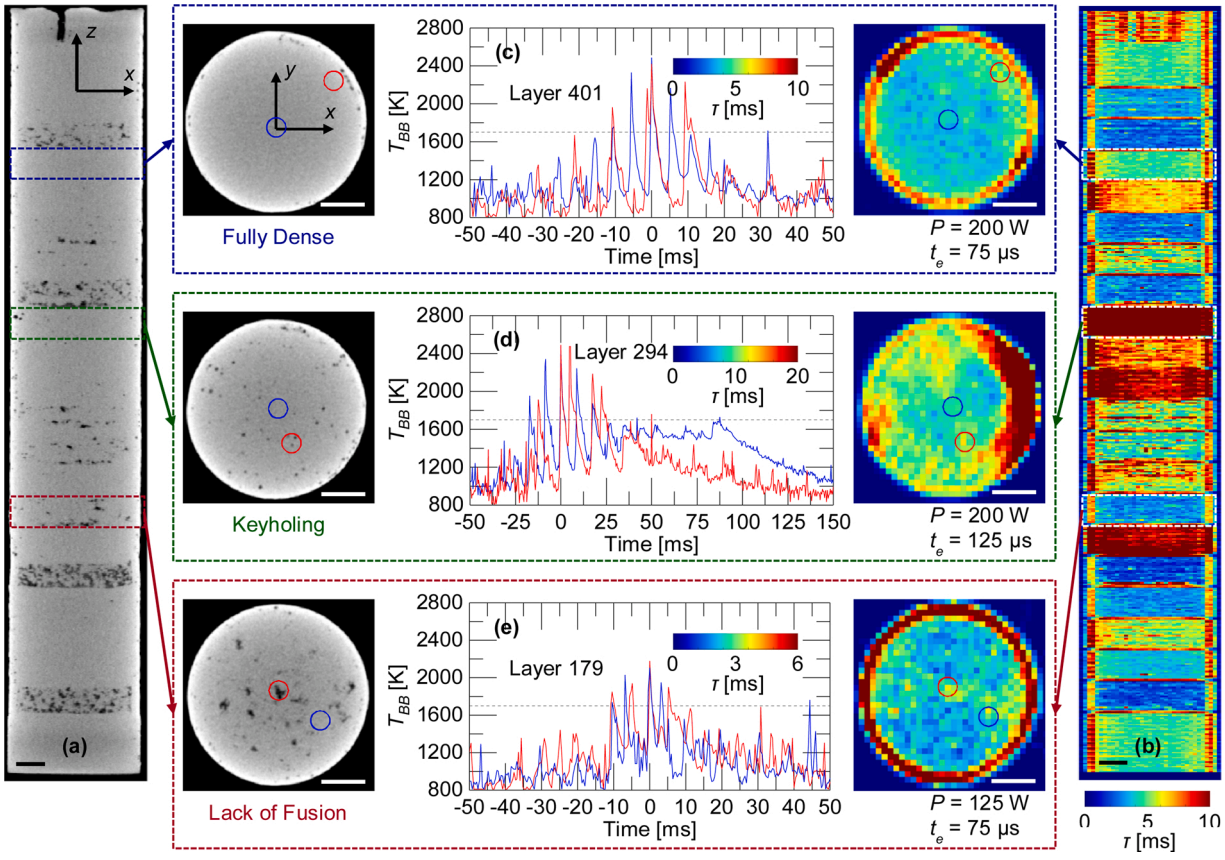

Fig. 4. Cylindrical sample (a) μCT data and (b) time above 1700 K thermal feature slices with representative layers and time series data for (c) fully dense, (d) keyholing, and (e) lack of fusion processing regimes. Scale bars, 1 mm. (For interpretation of the references to colour in this figure text, the reader is referred to the web version of this article.)

above 1700 K maps for representative layers are plotted with time series temperature data for two pixels, one without porosity (blue circles and corresponding temperature curves) and one with/near porosity (red circles and corresponding time series temperature curves). Fig. 4(c) has fully dense regime data from a layer manufactured with $P = 200$ W and $t_e = 75$ µs. This layer has 0 % interior porosity; however, the layer's µCT data in Fig. 4(c) shows porosity at the periphery where the laser corners. This is keyholing porosity caused by the laser's increased dwell time at points where the laser corners (Martin et al., 2019) and corresponds to an 11 % increase in the average time above 1700 K at the border region when excluding the border scans' contributions.

Fig. 4(d) shows the keyholing regime results from a layer processed with $P = 200$ W and $t_e = 125$ µs. The layer has stochastic keyholing porosity throughout it with a quantified interior porosity of 0.3 %. The expectation for this layer's thermal data is that the voxels that stay hotter longer will likely correspond to the keyholing porosity. However, Fig. 4(d) shows a case where the opposite occurs by the thermal history that corresponds to fully dense material staying hotter for a longer time after 50 ms. This result demonstrates the difficulty in distinguishing the fully dense thermal history from the thermal history where a keyholing pore was produced. Qualitative observation of the time above 1700 K thermal feature map further shows that high time above threshold values do not always correlate to keyholing pores. These results may be due to the fact that the keyholing pore occurred and stayed at the bottom of the melt pool which is two or more layer thicknesses down from the current layer. For example, the keyholing pore indicated by anomalies in layer 294's SWIR map would not be visible in the layer's µCT slice but instead in the µCT data for layer 292.

The µCT data and thermal data for a lack of fusion regime layer processed using $P = 125$ W and $t_e = 75$ µs are plotted in Fig. 4(e). This layer's porosity is also stochastic, and it has a porosity of 0.9 %. As seen for the keyholing regime layer, the time series data corresponding to the lack of fusion pore is difficult to distinguish from the fully dense thermal history. Also, the thermal feature map has various areas of higher time above 1700 K (in this case greater than 3 ms) with some of those areas corresponding to pores and some appearing fully dense in the µCT data. This may be explained by the effects of re-melting from subsequent layers driving differences between the µCT data's porosity and time above 1700 K's anomalies. The difficulties in locally correlating the porosity with thermal history shown in Fig. 4 for the fully dense, keyholing, and lack of fusion processing regimes demonstrate the need for a method to generate thermal feature-based porosity probability maps.

3.2. Single thermal feature porosity probability maps

Fig. 5 contains the probability density functions calculated from the cylindrical sample's classified thermal features and the resulting thermal feature porosity probability maps for the time above threshold (1700 K) and the maximum temperature. The cylindrical sample's time above 1700 K probability density functions are plotted in Fig. 5(a) and (b). Fig. 5(a) shows $P(\tau)$ for the sample's interior in red and for its border in blue. A comparison of the $P(\tau)$ probability density functions shows the time above 1700 K border mean (5.29 ms) is larger than the interior data mean (3.96 ms). The larger time above 1700 K mean at the border is caused by the increased dwell time when the laser corners and scans the border, thus, re-melting the sample's edges. Fig. 5(b) plots the interior $P(\varphi \cap \tau)$ in red and the border $P(\varphi \cap \tau)$ in blue. Note the difference in the y-axis ranges for the plots in Fig. 5. It can be seen that 91 % of the interior $P(\varphi \cap \tau)$ occurs below a time above 1700 K of 3.96 ms. This low time above threshold suggests most of the interior porosity correlates to

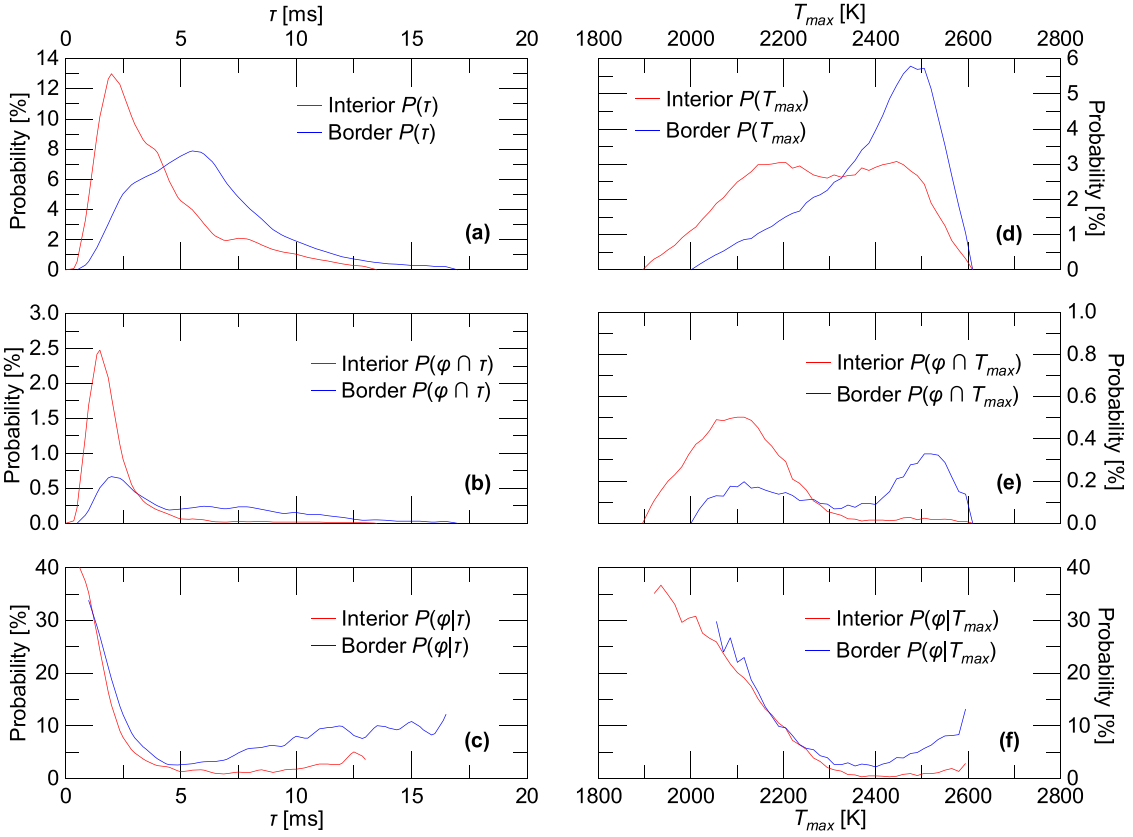

Fig. 5. (a) Time above 1700 K probability density function, (b) time above 1700 K and porosity intersection probability density function, (c) time above 1700 K porosity probability map calculated by Eq. 1, (d) maximum temperature probability density function, (e) maximum temperature and porosity intersection probability density function, and (f) maximum temperature porosity probability map calculated by Eq. 2 determined from the cylindrical sample's registered interior and border thermal feature data. (For interpretation of the references to colour in this figure text, the reader is referred to the web version of this article.)

lack of fusion from insufficient energy input. The border $P(\varphi \cap \tau)$ has 43 % of the data above a time above 1700 K of 5.29 ms. This high time above threshold suggests that keyholing causes a significant amount of porosity at the border region (4.7 % total border porosity).

Fig. 5(c) plots the time above 1700 K porosity probability maps, $P(\varphi|\tau)$, for the interior (red) and border (blue) regions. From low to high time above 1700 K, the porosity probabilities start high, decrease to a minimum, and then increase. The slope magnitude for the decreasing region is higher than that for the increasing region. Also, the curves for the interior and border maps are similar in the decreasing region. From the results in Fig. 5(b), lack of fusion causes the high porosity probabilities for time above 1700 K less than 5 ms, and this occurs for both the border and interior data. Most of the lack of fusion occurring over a narrow time above 1700 K range (0.5 ms–3.96 ms) produces the high slope magnitudes. The maps' low porosity probability regions correspond to the fully dense processing regime. As discussed for Fig. 5(b), keyholing causes the increases in porosity probability past a time above 1700 K of 5 ms, and this occurs with a higher rate for the borders due to the increased laser dwell time during cornering increasing the keyhole depth and instability.

Fig. 5(d) shows the cylindrical sample's maximum temperature probability density functions, $P(T_{max})$. The maximum temperature border data mean is 2400 K and the interior data mean is 2280 K. The border data's maximum temperature mean is larger because the high energy input form the border scan's laser parameters ($P = 150$ W, $t_e = 75$ µs, $d_p = 20$ µm). Fig. 5(e) contains the $P(\varphi \cap T_{max})$ probability density functions. It can be seen that 95 % of the interior $P(\varphi \cap T_{max})$ data occur below a maximum temperature of 2280 K, while only 49 % of the border $P(\varphi \cap T_{max})$ data occur below a maximum temperature of 2400 K. The maximum temperature porosity probability maps, $P(\varphi|T_{max})$, for the interior and border regions are plotted in Fig. 5(f). The maximum temperature porosity probability maps' trends in Fig. 5(f) follow those discussed for the time above 1700 K maps in Fig. 5(c). From low to high maximum temperature, both the interior and border maps start at a high porosity probability, decrease to a minimum around 2400 K, and then increase. This corresponds to the processing regime transition from lack of fusion to fully dense to keyholing. In both Fig. 5(c) and (f), the interior and border porosity probabilities are similar for the lack of fusion region because the porosity occurs independent of scan path effects at low energy inputs. The keyholing region maps are different because the effects of the laser cornering for the high energy inputs increase the keyholing depth and the likelihood for porosity formation.

3.3. 2D thermal feature space porosity probability maps

Fig. 6 contains 2D thermal feature space porosity probability maps obtained by combining information from the cylindrical sample's registered time above 1700 K and maximum temperature data. The plots in Fig. 6 permit a better determination of the porosity probability since the map generation data is now spread over an additional thermal feature space instead of being collapsed to a single thermal feature dimension. The time above 1700 K and maximum temperature space porosity probability map, $P(\varphi|\tau \cap T_{max})$, for the sample's interiors is plotted in Fig. 6(a). From Fig. 6(a), there is a clear region for $T_{max} >$ 2300 K and $\tau_{1700} < 7.5$ ms with less than 2 % porosity probability. This region defines the interior's fully dense thermal feature space. As the maximum temperature decreases, the process enters the lack of fusion space and, as the time above 1700 K increases, the system enters the keyholing space.

Fig. 6(b) is the time above 1700 K and maximum temperature space porosity probability map, $P(\varphi|\tau \cap T_{max})$, for the sample's borders. The border porosity probability map's fully dense thermal feature space region is much smaller than the corresponding interior space. The region is defined by $T_{max} > 2350$ K and $\tau_{1700} < 5$ ms. As the time above 1700 K increases, the process enters a large keyholing space with higher porosity probabilities than the corresponding interior space. This is expected for the border map since that location is where a majority of keyholing porosity occurs. As the maximum temperature decreases from the narrow fully dense region, the process enters the lack of fusion space similar to the corresponding space in the interior map.

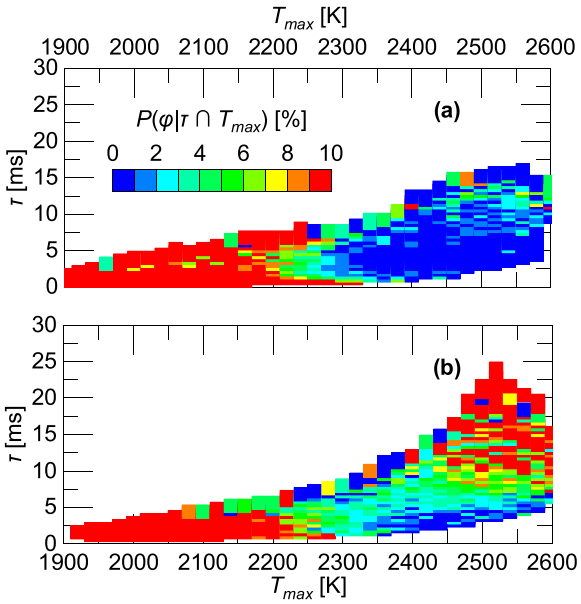

Fig. 6. Porosity probability maps for (a) interior and (b) border of cylindrical sample in time above 1700 K and maximum temperature space.

3.4. Complex sample porosity prediction

The complex sample is built with $P = 200$ W and $t_e = 75$ µs, which is a fully dense regime parameter set. The complex sample's time above 1700 K and maximum temperature data produced the 2D thermal feature histograms plotted in Fig. 7(a) and (b) by using the data from the sample's entire geometry which is shown by the time above threshold voxel reconstruction in Fig. 7(c). The interior data in Fig. 7(a) is clustered in the region corresponding to the minimum porosity probability in Fig. 6(a) as expected for a sample built by a fully dense regime parameter set. Fig. 7(b) shows there are some voxels in the complex sample's border data that have time above thresholds outside of the map

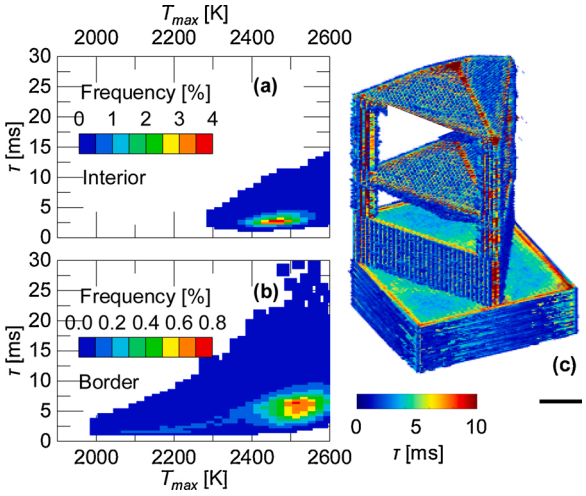

Fig. 7. (a) Interior and (b) border area time above 1700 K and maximum temperature 2D thermal feature histograms for entire volume of complex sample with (c) time above 1700 K based 3D voxel reconstruction. Scale bar, 2 mm.

generation space. This is due to the complex part's overhang boundary condition where its overhang portions experience a higher time above threshold.

The time above 1700 K and maximum temperature space porosity probability maps in Fig. 6 are used to demonstrate the capability to predict the complex sample's porosity. Fig. 8 compares the time above 1700 K and maximum temperature space porosity probability maps' prediction results of the complex sample with its μCT data starting with the sample's cross-section in Fig. 8(a). The porosity probability predictions and μCT data for three layers from the sample's various geometry section types are plotted below the cross-section data as Fig. 8 (b–d). The sample's three section types are supported pyramid (top half of pyramid structures), overhang pyramid (bottom half of pyramid structures), and bulk (i.e., the rectangular and triangular cross-sections), and are plotted in Fig. 8(b)–(d), respectively. Color coding highlights the *z*-direction (i.e., build direction) locations of the layers on the sample's μCT data cross-section. The μCT data shows the sample's porosity primarily occurred at its borders, which is characteristic of the keyholing porosity that occurs during fully dense regime processing as discussed for Fig. 4(c).

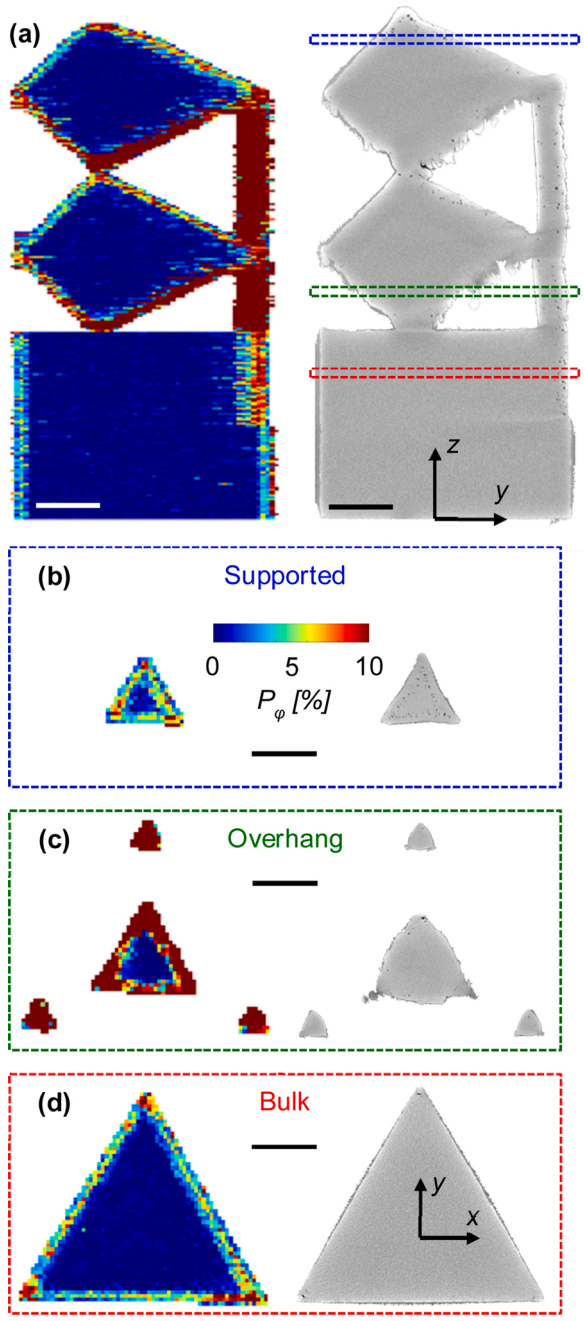

Fig. 8. Complex sample μCT data with corresponding porosity probability predictions using 2D time above 1700 K and maximum temperature maps for (a) sample cross-section and selected layers from (b) supported, (c) overhang, and (d) bulk geometries. Scale bars, 2 mm.

Fig. 8 shows the map from Fig. 6(a) generally predicts low porosity probabilities for the sample's interior regardless of cross-sectional geometry and overhang case. The average porosity probabilities predicted for the bulk sections' interiors, the supported pyramids' interiors, and the overhang pyramids' interiors are 0.2 %, 0.4 %, and 0.9 %, respectively. The low porosity values predicted for the complex sample's interiors match the expectations for the fully dense processing regime. Also as expected, the average predicted porosity probabilities increase for the sample sections' borders. The average predicted border porosity probabilities for the rectangular and triangular cross-sections, supported pyramids, and overhang pyramids are 4 %, 5 %, and 11 %, respectively. The increase in porosity probability for the overhang pyramids' border area is due to differences in the thermal boundary conditions. The overhang pyramids' exterior surfaces are melted over powder, which causes slower cooling (correlating to higher time above thresholds) and geometry deviations as revealed by the μCT data in Fig. 8(a). These effects are expected to negatively impact the prediction success for the overhang pyramids' border regions like shown in Fig. 8(c) since the porosity probability maps are only generated with data from bulk material. Future porosity probability map generation should include data from overhang boundary conditions.

3.5. Porosity prediction scoring

Fig. 9 demonstrates the ROC development process over an operating point (i.e., threshold for assigning voxels as porosity or fully dense) range from 0 % to 40 % porosity probability for the maximum temperature only map's porosity prediction results. The true positive rate (blue) and false positive rate (red) are plotted as a function of the operating point in Fig. 9(a). Both the true and false rates start at one and then follow different curves as they decrease to zero at higher operating

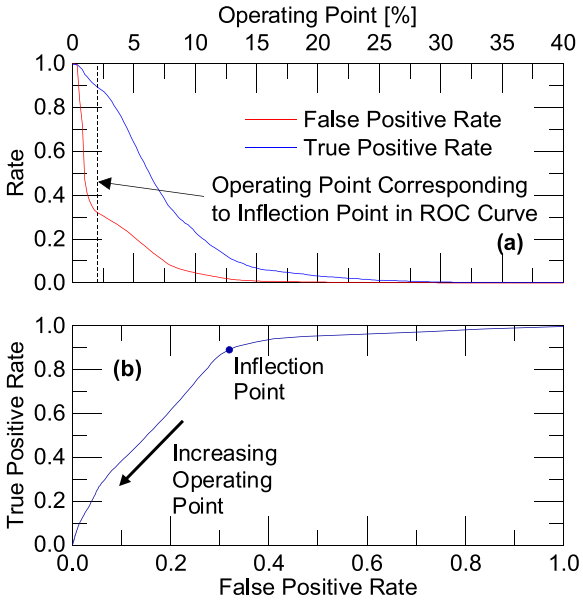

Fig. 9. (a) Complex sample porosity probability prediction false positive and true positive rates at various operating points for maximum temperature map with (b) corresponding ROC curve. (For interpretation of the references to colour in this figure text, the reader is referred to the web version of this article.)

points. For very low operating points, nearly every voxel in the predictions will be assigned as porosity, producing high true and false positive rates. The rates fall with increasing operating point because less good data and more bad data are flagged as defective. The spread between the true positive rate and false positive rate corresponds to the performance of the prediction map, and it is quantified through the ROC plot in Fig. 9(b). The ROC curve describes the performance of the porosity probability map, with more accurate predictions producing curves shifted up and to the left. A perfect detector will produce an ROC curve that only contains true positive rates of one and false positive rates of zero, regardless of the operating point. Real detectors produce an ROC with an inflection point, i.e., the point that maximizes the difference between true and false positive rates. Here, the inflection point for the maximum temperature porosity probability map occurs at a 2.0 % porosity operating point and corresponds to a true positive rate of 0.89, and a false positive rate of 0.32. The Area Under the Curve (AUC) for the maximum temperature porosity map's ROC curve is 0.82. The maximum temperature porosity map's AUC is 64 % better than tests having no ability to make predictions (i.e., AUC = 0.5) and 22 % away from being a perfect test (i.e., AUC = 1).

Fig. 10 compares the prediction performance of the various porosity probability maps. The ROC curves for the time above threshold only maps' predictions are plotted in Fig. 10(a) with a shared legend in Fig. 10(b). The ROC curves in Fig. 10(a) show that prediction performance increases for higher thresholds up to 2100 K. This is because increasing the temperature threshold for time above threshold extraction produces porosity probability maps with increased sensitivity for the keyholing regime and less sensitivity to boundary condition effects like the overhangs. Predictions are not made for time above thresholds past 2100 K because the porosity probability maps' thermal feature space collapses to 0 ms. The 1100 K and 1300 K maps perform the worst with the false positive exceeding the true positive rate for all operating points, i.e., the curves fall below the line with a slope of unity. This is because the process noise's contribution to the time above threshold measurements extracted at low temperatures decreases the feature's quality, which drastically reduces the resulting porosity probability map's sensitivity. As an example of noise, laser spatter that occurs during processing can significantly affect the time above threshold calculation at low extraction temperatures. The laser spatter randomly causes an artificial increase in the time above threshold that carries forward to negatively impact the porosity probability maps.

The ROC curves for the predictions made by the 2D porosity probability maps in time above threshold and maximum temperature space are plotted in Fig. 10(b). The combined maps provide predictions with similar ROC curves regardless of the temperature threshold. The ROC curves' AUC values are plotted in Fig. 10(c) where their results are compared to the maximum temperature only porosity probability map's AUC. The data are plotted as a function of the time above threshold extraction temperature. The time above threshold only maps predictions' AUC approach the maximum temperature result with increasing threshold. As the threshold increases, the AUC increases because the higher temperature extraction threshold produces porosity probability maps with higher sensitivities as discussed for Fig. 10(a). The 2D feature space maps predictions' AUC are insensitive to temperature extraction threshold for their time above threshold component and slightly outperform the maximum temperature only prediction's AUC by an average of 3 %. This is because all the 2D porosity probability maps like in Fig. 6 have clearly defined regions of fully dense regime thermal feature space, lack of fusion space, and keyholing space regardless of the temperature extraction threshold for the time above threshold, which is not the case for all the time above threshold only maps. The results in Fig. 10 indicate that the maximum temperature is a dominant feature for predicting porosity. Including the time above threshold in the 2D feature space predictions adds additional information that slightly increases the maps' performance. These results also reveal the capability of the porosity probability mapping framework to evaluate the ability of a thermal feature to predict porosity.

The ROC curve construction is performed on a section-by-section basis for the complex sample. The bulk, overhang pyramid, and supported pyramid sections are analyzed using the maximum temperature map and the time above 1500 K combined maps since they perform best for the entire sample. Fig. 11 contains the sectioned ROC curves for those maps' predictions with the sample's sections highlighted on the maximum temperature prediction slice inset in Fig. 11(a). The bulk, overhang, and supported sections' ROC curves are plotted in red, green,

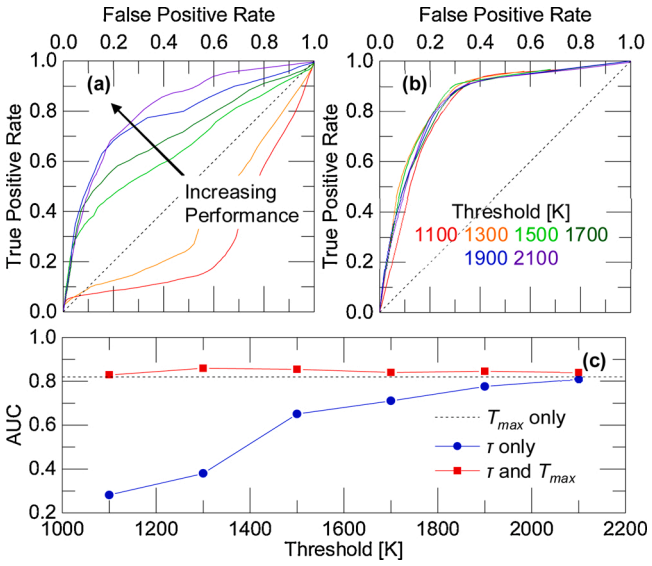

Fig. 10. ROC curves for (a) time above threshold only and (b) 2D time above threshold and maximum temperature porosity probability maps (key in (b) shared with (a)) with (c) AUC for maximum temperature only, time above threshold only, and 2D maps as functions of threshold.

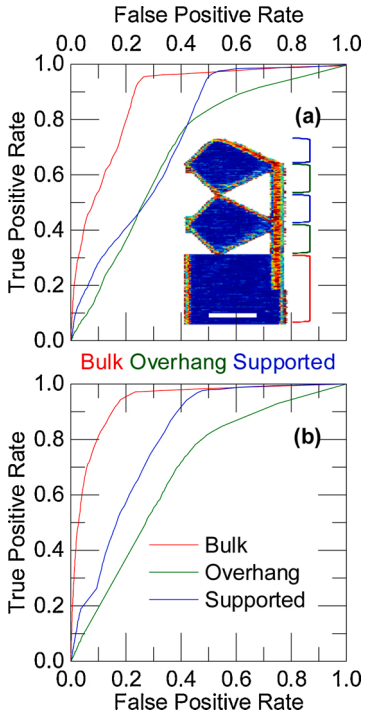

Fig. 11. ROC curves from (a) maximum temperature and (b) 2D maximum temperature and time above 1500 K porosity probability maps. Scale bar, 4 mm. (For interpretation of the references to colour in this figure text, the reader is referred to the web version of this article.)

and blue, respectively. Fig. 11(a) shows the maximum temperature only map's ROC results. Fig. 11(b) consists of the 2D thermal feature space ROC curves.

The curves in Fig. 11(a) and (b) demonstrate that both maps perform better for the bulk and supported pyramid data than for the overhang pyramid data. The maps' performances are best for the bulk section because that geometry type has scan pathing and heat transfer boundary conditions that match the generation data. The supported sections have the next best ROC performance because that geometry type has thermal boundary conditions that match the map generation data. However, the changing cross-sectional area does negatively impact the predictions for the complex sample's supported sections when the area decreases below that of the cylindrical sample. This is because the short scan vectors for the complex sample's layers with the smaller areas drive thermal variations that are not well accounted for in the map generation data. The ROC results for the bulk and supported pyramid sections in Fig. 11 clearly show the 2D feature space map provides more accurate predictions than the maximum temperature only map due to the additional information provided by the time above threshold. These results are further quantified by calculating the AUCs for each curve in Fig. 11, which are listed in Table 1.

There is an average increase of 8 % in the AUC for the 2D feature space map's predictions for the bulk and supported pyramid sections compared to the maximum temperature only predictions. Both porosity probability maps perform worse for the overhang pyramids when compared to the bulk sections due to the absence of map generation data for the overhang boundary condition. For example, the maximum temperature only prediction's AUC for the overhang sections is 22 % smaller than the bulk sections. The 2D feature space's AUC is 27 % smaller for the overhang pyramid sections when compared to that map's predictions for the bulk sections. These results demonstrate that the difference in thermal boundary condition significantly affects the thermal features which causes the overhang data to reduce the performance for all maps analyzed in this study. This can be overcome in the future by using the methods presented in this paper because they are readily adaptable to generate porosity probability maps from SWIR thermal data and μCT data acquired for complex geometry cases. Additionally, keyhole pore offsetting in the z-direction due to the trapping of pores at the bottom of the melt pool is a common phenomenon that may reduce the maps' performances. This is because the current porosity probability maps do not consider layer-to-layer effects like keyhole pore offsetting. Accounting for the keyhole forming one or more layers down by incorporating thermal features and μCT data from adjacent layers during map generation should produce maps that are more sensitive to that porosity type, thus, increasing their performance.

4. Summary and conclusions

This paper developed a porosity probability mapping methodology based on SWIR imaging thermal features and μCT data. The methodology produced porosity probability maps that span the lack of fusion, keyholing, and fully dense processing regimes for LPBF of 304 L stainless steel by using SWIR data and μCT data. The porosity captured in the maps were generated by solely adjusting the laser parameters (i.e., the power and the exposure time/scan speed) in a very simple geometry. Because certain process parameters are far more likely to generate defects, this allowed a rapid compilation of maps between thermal features and porosity. While the interaction between the process parameters and the geometry in more complicated specimens leads to defects under different conditions, the porosity probability maps prove to be representative. For the complex geometry fabricated with nominal properties, an AUC of 0.94 is achieved for internal regions. This drops to an AUC of 0.69 for overhanging regions and 0.81 for supported regions. These results show both the potential as well as the limitations of extrapolating thermal feature maps in the absence of geometric information. This paper also demonstrated that while the maximum temperature, T_{max}, thermal feature significantly outperformed the time above the threshold feature, τ, the effectiveness of the algorithm was appreciably improved (AUC from 0.88 to 0.94) by including τ with the appropriate threshold.

Table 1
AUC for maximum temperature and 2D maximum temperature and time above 1500 K porosity probability models based on each complex sample section.

Section	T_{max} AUC	τ_{1500} and T_{max} AUC
Bulk	0.88	0.94
Overhang	0.69	0.69
Supported	0.74	0.81

In an industrial application, the best forming porosity probability map can potentially identify porosity with a true positive rate of 0.9 at a false positive rate of 0.15 for bulk material. While this result is promising, it suggests that the overall performance can be increased by incorporating additional geometric dependent maps (e.g., thin wall structures, interior/exterior border subregions, and up/down-facing boundaries). The data to generate these mappings may be obtained in a production setting for real geometries. This would build up sufficient data to establish the correlations following the procedure in this paper. The techniques can also be expanded to incorporate additional thermal features which may further improve the state estimation. These steps will continuously improve the methodology's robustness to the point that it can be used for industrial validation.

CRediT authorship contribution statement

Cody S. Lough: Conceptualization, Methodology, Investigation, Formal analysis, Writing - original draft. **Tao Liu:** Investigation. **Xin Wang:** Software, Methodology. **Ben Brown:** Investigation, Resources. **Robert G. Landers:** Conceptualization, Writing - review & editing. **Douglas A. Bristow:** Conceptualization. **James A. Drallmeier:** Supervision. **Edward C. Kinzel:** Conceptualization, Writing - review & editing, Supervision.

Declaration of Competing Interest

Edward Kinzel reports financial support was provided by Honeywell Federal Manufacturing and Technologies LLC.

Acknowledgments

This work was funded by Honeywell Federal Manufacturing & Technologies under Contract No. DE-NA0002839 with the U.S. Department of Energy. The United States Government retains and the publisher, by accepting the article for publication, acknowledges that the United States Government retains a nonexclusive, paid up, irrevocable, world-wide license to publish or reproduce the published form of this manuscript, or allow others to do so, for the United States Government purposes.

References

Bartlett, J.L., Heim, F.M., Murty, Y.V., Li, X., 2018. In situ defect detection in selective laser melting via full-field infrared thermography. Addit. Manuf. 24, 595–605. https://doi.org/10.1016/j.addma.2018.10.045.

Cheng, B., Lydon, J., Cooper, K., Cole, V., Northrop, P., Chou, K., 2018. Infrared thermal imaging for melt pool analysis in SLM: a feasibility investigation. Virtual Phys. Prototyp. 13, 8–13. https://doi.org/10.1080/17452759.2017.1392685.

Coeck, S., Bisht, M., Plas, J., Verbist, F., 2019. Prediction of lack of fusion porosity in selective laser melting based on melt pool monitoring data. Addit. Manuf. 25, 347–356. https://doi.org/10.1016/j.addma.2018.11.015.

Craeghs, T., Clijsters, S., Kruth, J.P., Bechmann, F., Ebert, M.C., 2012. Detection of process failures in layerwise laser melting with optical process monitoring. Phys. Procedia 39, 753–759. https://doi.org/10.1016/j.phpro.2012.10.097.

Forien, J.B., Calta, N.P., DePond, P.J., Guss, G.M., Roehling, T.T., Matthews, M.J., 2020. Detecting keyhole pore defects and monitoring process signatures during laser powder bed fusion: a correlation between in situ pyrometry and ex situ X-ray

radiography. Addit. Manuf. 35, 101336 https://doi.org/10.1016/j.addma.2020.101336.

Gong, H., Rafi, K., Gu, H., Starr, T., Stucker, B., 2014. Analysis of defect generation in Ti-6Al-4V parts made using powder bed fusion additive manufacturing processes. Addit. Manuf. 1, 87–98. https://doi.org/10.1016/j.addma.2014.08.002.

Gordon, J.V., Narra, S.P., Cunningham, R.W., Liu, H., Chen, H., Suter, R.M., Beuth, J.L., Rollett, A.D., 2020. Defect structure process maps for laser powder bed fusion additive manufacturing. Addit. Manuf. 36, 101552 https://doi.org/10.1016/j.addma.2020.101552.

Gould, B., Wolff, S., Parab, N., Zhao, C., Lorenzo-Martin, M.C., Fezzaa, K., Greco, A., Sun, T., 2021. In situ analysis of laser powder bed fusion using simultaneous high-speed infrared and X-ray imaging. JOM 73, 201–211. https://doi.org/10.1007/s11837-020-04291-5.

Heigel, J.C., Whitenton, E., 2018. Measurement of thermal processing variability in powder bed fusion. In: Proc. - 2018 ASPE euspen Summer Top. Meet. Adv. Precis. Addit. Manuf., 69, pp. 242–247.

Hojjatzadeh, S.M.H., Parab, N.D., Guo, Q., Qu, M., Xiong, L., Zhao, C., Escano, L.I., Fezzaa, K., Everhart, W., Sun, T., Chen, L., 2020. Direct observation of pore formation mechanisms during LPBF additive manufacturing process and high energy density laser welding. Int. J. Mach. Tools Manuf. 153, 103555 https://doi.org/10.1016/j.ijmachtools.2020.103555.

King, W.E., Barth, H.D., Castillo, V.M., Gallegos, G.F., Gibbs, J.W., Hahn, D.E., Kamath, C., Rubenchik, A.M., 2014. Observation of keyhole-mode laser melting in laser powder-bed fusion additive manufacturing. J. Mater. Process. Technol. 214, 2915–2925. https://doi.org/10.1016/j.jmatprotec.2014.06.005.

Krauss, H., Zeugner, T., Zaeh, M.F., 2014. Layerwise monitoring of the Selective Laser Melting process by thermography. Phys. Procedia 56, 64–71. https://doi.org/10.1016/j.phpro.2014.08.097.

Lough, C.S., Wang, X., Smith, C.C., Landers, R.G., Bristow, D.A., Drallmeier, J.A., Brown, B., Kinzel, E.C., 2020. Correlation of SWIR imaging with LPBF 304L stainless steel part properties. Addit. Manuf. 35 https://doi.org/10.1016/j.addma.2020.101359.

Martin, A.A., Calta, N.P., Khairallah, S.A., Wang, J., Depond, P.J., Fong, A.Y., Thampy, V., Guss, G.M., Kiss, A.M., Stone, K.H., Tassone, C.J., Nelson Weker, J., Toney, M.F., van Buuren, T., Matthews, M.J., 2019. Dynamics of pore formation during laser powder bed fusion additive manufacturing. Nat. Commun. 10, 1–10. https://doi.org/10.1038/s41467-019-10009-2.

Mireles, J., Ridwan, S., Morton, P.A., Hinojos, A., Wicker, R.B., 2015. Analysis and correction of defects within parts fabricated using powder bed fusion technology. Surf. Topogr. Metrol. Prop. 3 https://doi.org/10.1088/2051-672X/3/3/034002.

Mitchell, J.A., Ivanoff, T.A., Dagel, D., Madison, J.D., Jared, B., 2020. Linking pyrometry to porosity in additively manufactured metals. Addit. Manuf. 31 https://doi.org/10.1016/j.addma.2019.100946.

Mohr, G., Altenburg, S.J., Ulbricht, A., Heinrich, P., Baum, D., Maierhofer, C., Hilgenberg, K., 2020. In-situ defect detection in laser powder bed fusion by using thermography and optical tomography—comparison to computed tomography. Metals (Basel) 10. https://doi.org/10.3390/met10010103.

Promoppatum, P., Srinivasan, R., Quek, S.S., Msolli, S., Shukla, S., Johan, N.S., van der Veen, S., Jhon, M.H., 2022. Quantification and prediction of lack-of-fusion porosity in the high porosity regime during laser powder bed fusion of Ti-6Al-4V. J. Mater. Process. Technol. 300, 117426 https://doi.org/10.1016/j.jmatprotec.2021.117426.

Taherkhani, K., Sheydaeian, E., Eischer, C., Otto, M., Toyserkani, E., 2021. Development of a defect-detection platform using photodiode signals collected from the melt pool of laser powder-bed fusion. Addit. Manuf. 46 https://doi.org/10.1016/j.addma.2021.102152.

Wang, W., Ning, J., Liang, S.Y., 2021. Prediction of lack-of-fusion porosity in laser powder-bed fusion considering boundary conditions and sensitivity to laser power absorption. Int. J. Adv. Manuf. Technol. 112, 61–70. https://doi.org/10.1007/s00170-020-06224-7.

Yavari, R., Riensche, A., Tekerek, E., Jacquemetton, L., Halliday, H., Vandever, M., Tenequer, A., Perumal, V., Kontsos, A., Smoqi, Z., Cole, K., Rao, P., 2021. Digitally twinned additive manufacturing: detecting flaws in laser powder bed fusion by combining thermal simulations with in-situ meltpool sensor data. Mater. Des. 211, 110167 https://doi.org/10.1016/j.matdes.2021.110167.

Yoder, S., Nandwana, P., Paquit, V., Kirka, M., Scopel, A., Dehoff, R.R., Babu, S.S., 2019. Approach to qualification using E-PBF in-situ process monitoring in Ti-6Al-4V. Addit. Manuf. 28, 98–106. https://doi.org/10.1016/j.addma.2019.03.021.